Viscous dissipation and dynamics in simulations of rotating, stratified plane-layer convection

Simon R. W. Lance [ORCID],[1]★ Laura K. Currie [ORCID][2] and Matthew K. Browning [ORCID][1]★

[1]*Physics and Astronomy Department, University of Exeter, Stocker Rd, Exeter EX4 4QL, UK*
[2]*Department of Mathematical Sciences, Durham University, Durham DH1 3LE, UK*

ABSTRACT

Convection in stars and planets must be maintained against viscous and Ohmic dissipation. Here, we present the first systematic investigation of viscous dissipation in simulations of rotating, density-stratified plane layers of convection. Our simulations consider an anelastic ideal gas, and employ the open-source code Dedalus. We demonstrate that when the convection is sufficiently vigorous, the integrated dissipative heating tends towards a value that is independent of viscosity or thermal diffusivity, but depends on the imposed luminosity and the stratification. We show that knowledge of the dissipation provides a bound on the magnitude of the kinetic energy flux in the convection zone. In our non-rotating cases with simple flow fields, much of the dissipation occurs near the highest possible temperatures, and the kinetic energy flux approaches this bound. In the rotating cases, although the total integrated dissipation is similar, it is much more uniformly distributed (and locally balanced by work against the stratification), with a consequently smaller kinetic energy flux. The heat transport in our rotating simulations is in good agreement with results previously obtained for 3D Boussinesq convection, and approaches the predictions of diffusion-free theory.

Key words: convection – hydrodynamics – stars: interiors.

1 INTRODUCTION

Convection occurs in the interior of every main-sequence star and in many planets, and must be maintained against a finite amount of viscous and Ohmic dissipation. In a steady state, the dynamics and the dissipation are therefore linked; constraints on one yield constraints on the other.

Many authors have explored this link. For example, the widely employed theory of Rayleigh–Bénard convection developed by Grossmann & Lohse (2000) relies on the exact relationship between viscous dissipation and heat transport (Shraiman & Siggia 2000); in their model, the heat transport depends crucially on whether the viscous and thermal dissipation occur primarily in the bulk of the convective domain or in the boundary layers that form at its top and base. Jones, Mizerski & Kessar (2022) have recently explored an extension of this theory to the density-stratified case, with the spatial distribution of the dissipation again playing a vital role. In the stellar context, Anders et al. (2022) have shown that the magnitude of the dissipation within a convection zone strongly influences the amount of convective overshooting into adjacent stable layers. The form and magnitude of the dissipation are likewise crucial in a variety of efforts to go 'beyond mixing length theory' (MLT) (e.g. Canuto 1997; Viallet et al. 2013; Kupka, Ahlborn & Weiss 2022; Meakin & Arnett 2010, Arnett et al. 2015). In the Sun, where the form and magnitude

of convective flows in the deep convection zone are currently the subject of much debate (e.g. Vasil, Julien & Featherstone 2021), the total dissipation may provide important constraints on the flows (Ginet 1994). Ohmic dissipation, in particular, is thought to limit the depth of zonal winds in Jupiter (Liu, Goldreich & Stevenson 2008; Kaspi et al. 2018, 2020), may constrain magnetism in the interiors of low-mass stars (Browning et al. 2016), and could influence the radii of hot Jupiters (Batygin & Stevenson 2010).

The purpose of this paper is to provide new constraints on the magnitude and spatial distribution of the viscous dissipation that may be occurring in stellar convection zones. Few prior works have systematically investigated this in the astrophysically relevant case of a gas with density and temperature stratification, and none have done so when rotation is also present. Here, we study this issue within one of the simplest possible systems that captures convection, rotation, and stratification, by conducting a series of hydrodynamic simulations of stratified (anelastic) convection in a rotating Cartesian domain, situated at a fixed latitude. The vast majority of the simulations presented here are 2D, although we compare some of these results to a very small number of 3D simulations. Many elements that are important in real stars – including, crucially, magnetic fields – are thus absent here. However, this setup has the great advantage that it allows us to sample parameter regimes that would be difficult or impossible to probe in equivalent detail in a full 3D spherical geometry.

In particular, we are able to assess how the dissipation scales with luminosity, rotation rate, and stratification in the limit where the diffusivities are small (i.e. when the convective supercriticality is

★ E-mail: m.k.m.browning@exeter.ac.uk (MKM);
laura.currie@durham.ac.uk (SRWL)

high). In what follows, we argue that in this regime the dissipation rate (integrated over the convection zone) depends only on the luminosity and the stratification, and is (at fixed supercriticality) independent of rotation. However, the spatial distribution of this dissipation – and with it, many other aspects of the dynamics – does depend on rotation, as detailed below.

In the remainder of this introduction, we summarize prior bounds on the viscous and Ohmic dissipation, and describe how our work extends these. In Section 2, we detail our simulation setup. In Section 3, we provide a brief, qualitative overview of the dynamics in our simulations. In Section 4, we examine the magnitude and spatial distribution of the dissipation in these simulations, and how these scale with the convective driving, the stratification, and the rotational influence. In Section 5, we explore the links between the dissipation, dynamics, and heat transport. We show there that knowledge of the dissipation provides novel constraints on the kinetic energy flux. We close in Section 6 with a summary of our results and their possible astrophysical implications.

1.1 Overview of prior work: bounds and constraints on dissipative heating

In the interior of a star, the microphysical diffusion of momentum, heat, or magnetic fields is typically very small compared to other physical processes, so that the relevant non-dimensional numbers (e.g. the Reynolds, Rayleigh, and magnetic Reynolds numbers) are usually very large (e.g. Kulsrud 2005; Brun & Browning 2017; Jermyn et al. 2022). This need not imply, however, that viscous and Ohmic dissipation are negligible.

To place our discussion on a firmer footing, and to highlight some of the aims of our work, we briefly describe the thermodynamic constraints on the dissipation here. More complete discussions can be found in Hewitt, McKenzie & Weiss (1975, hereafter HMW75), in Backus (1975), Alboussière & Ricard (2013, 2014), and Alboussière et al. (2022).

Consider a volume V of convecting fluid with an associated magnetic field $\mathbf{B}$, enclosed by some surface S. Assume this surface is impenetrable and either stress-free or no-slip, so that the normal component of the fluid velocity $\mathbf{u}$, and either all components of $\mathbf{u}$ or the tangential stress vanish on S. The local rate of change of total energy can be expressed by

$$\frac{\partial}{\partial t}\left(\rho e + \frac{1}{2}\rho u^2 + \frac{B^2}{2\mu_0} - \rho\Psi\right)$$
$$= -\nabla \cdot \left[\rho\left(e + \frac{1}{2}u^2 - \Psi\right)\mathbf{u} + \frac{(\mathbf{E} \times \mathbf{B})}{\mu_0} + P\mathbf{u} - \tau \cdot \mathbf{u} - k\nabla T\right] + H$$

(1)

with e the fluid's internal energy, ρ its density, Ψ the gravitational potential satisfying $\mathbf{g} = \nabla\Psi$, P the pressure, τ_{ij} is the contribution to the total stress tensor from irreversible processes, k is the thermal conductivity, T is the temperature, H is the rate of internal heat generation (e.g. by nuclear fusion or radioactive decay) or cooling (e.g. by any processes not included in the conductive term), and μ_0 is the permeability of free space. We have assumed the MHD approximation holds, so that $E = -u \times B + \eta\nabla \times B$, where $\eta = 1/(\mu_0\sigma)$ is the magnetic diffusivity and σ is the electrical conductivity (e.g. Priest 2014). Physically, the rate of total energy change at a point is given by the sum of the net inward flux of energy (the divergence terms in equation) and the rate of internal heat generation.

The first global constraint is that total energy is conserved, but this yields little insight into the magnitude of the dissipative heating.

Integrating (1) over V gives

$$\int_S k\frac{\partial T}{\partial x_i}\,\mathrm{d}S_i + \int_V H\,\mathrm{d}V = 0,$$

(2)

assuming both a steady state and that the electric current $\mathbf{j} = (\nabla \times \mathbf{B})/\mu_0$, vanishes everywhere outside V. Equation (2) implies that the net flux out of V is equal to the total rate of internal heating and cooling. But dissipative terms do not appear in this equation; viscous and ohmic heating do not contribute to the overall heat flux.

To constrain the dissipation, we turn instead to the internal energy equation, which can be written as

$$\rho\left(\frac{\partial e}{\partial t} + (\mathbf{u} \cdot \nabla)e\right) = \nabla \cdot (k\nabla T) - P(\nabla \cdot \mathbf{u})$$
$$+ \tau_{ij}\frac{\partial u_i}{\partial x_j} + \frac{j^2}{\sigma} + H.$$

(3)

Assuming a steady state and integrating over the fluid volume V, it can be shown that

$$\int_V (\mathbf{u} \cdot \nabla)P\mathrm{d}V + \Phi = 0$$

(4)

where the total dissipative heating rate, Φ, is defined as

$$\Phi = \int_V \left(\tau_{ij}\frac{\partial u_i}{\partial x_j} + \frac{j^2}{\sigma}\right)\mathrm{d}V.$$

(5)

The first and second terms inside the integral represent the contributions due to viscous and Ohmic effects, respectively. Equation (4) implies that the total dissipative heating, integrated over the volume, is exactly balanced by the work done against the background stratification (Currie & Browning 2017).

Equivalently, from the first law of thermodynamics, we have

$$T\mathrm{d}S = \mathrm{d}e - \frac{P}{\rho^2}\mathrm{d}\rho$$

(6)

where s is the specific entropy, implying that

$$\rho T\left(\frac{\partial s}{\partial t} + (\mathbf{u} \cdot \nabla)s\right) = \nabla \cdot (k\nabla T) + \tau_{ij}\frac{\partial u_i}{\partial x_j} + \frac{j^2}{\sigma} + H.$$

(7)

Following HMW75, we can divide this equation by T, and integrate over volume to find

$$\int_S \frac{k}{T}\nabla T \cdot \mathrm{d}S + \int_V k\left|\frac{\nabla T}{T}\right|^2 \mathrm{d}V + \int_V \frac{1}{T}\left(H + \tau_{ij}\frac{\partial u_i}{\partial x_j} + \frac{j^2}{\sigma}\right)\mathrm{d}V = 0.$$

(8)

Physically, this equation expresses the fact that there is a flux of entropy in and out of the domain (first term), and that entropy can be generated in the bulk by conduction (second term) or by heating within the domain (third term). If the inward flux of entropy at the bottom is less than the outward flux of entropy out the top – as occurs if there is a temperature contrast across the domain – then the difference must be made up by entropy generation in the convection zone (either by conduction or dissipation).

In HMW75, this equation is used to derive an upper limit on the total amount of dissipative heating that can occur in a convective layer of depth d. This is given by

$$E \equiv \frac{\Phi}{L} < \frac{T_0 - T_{\mathrm{top}}}{T_{\mathrm{top}}},$$

(9)

where T_{top} and T_0 denote the upper and lower boundary values of the temperature, respectively, and L is the luminosity through the layer. This upper limit corresponds to the case in equation (8) where there is negligible entropy generation by conduction or heating, and where the dissipation occurs at the highest possible temperature (i.e. at the bottom of the domain). In this case, as discussed in HMW75, the

total dissipative heating rate is bounded not by L, but by $L\,d/H_T$, with H_T a suitably defined temperature scale height.

In general, however, it cannot be assumed that dissipation occurs at the highest possible temperatures. For example, the dissipation could be distributed more uniformly throughout the layer, or it could be concentrated predominantly in boundary layers. In these situations, E could, in principle, be much smaller than the upper bound of equation (9).

Prior simulations have shown that in certain circumstances convection can approach a version of this bound. HMW75 demonstrated that for the specific case of a Boussinesq liquid without magnetism, the integrated dissipation approached a value of order the bound at high enough Rayleigh numbers Ra (measuring the ratio of buoyancy driving to viscous and thermal dissipation). Jarvis & McKenzie (1980) expanded on this by investigating the case of compressible convection in the infinite Prandtl number Pr (defined as the ratio of viscous to thermal diffusivities) regime, appropriate for convection within the Earth's mantle. Currie & Browning (2017, hereafter CB17) extended these results to a gas at finite Pr, as appropriate for convection in stellar interiors. In a series of 2D hydrodynamic simulations without rotation, they found that the total dissipative heating in their calculations obeyed a tighter, but purely empirical bound, specifically (defining $E \equiv \Phi/L$, with Φ is the total viscous heating and L is the luminosity)

$$E = \frac{\mathrm{d}}{\hat{H}_T} \tag{10}$$

where

$$\hat{H}_T = \frac{H_{T,0}H_{T,\mathrm{top}}}{H_{T,z^*}} \tag{11}$$

is a modified thermal scale height involving the scale height at the top and bottom boundaries ($H_{T,\mathrm{top}}$ and $H_{T,0}$, respectively), and some vertical height z^*, defined such that half of the fluid mass lies above and below z^*. They showed that for sufficiently high supercriticalities, the value of E appeared to approach equation (10) asymptotically.

Yet not all convective systems actually approach these upper bounds. Recently Alboussière et al. (2022), studying 2D convection with an unusual equation of state in which entropy was a function solely of density, found much lower levels of dissipation than suggested by equation (10) in most cases. They attributed the difference in part to the different boundary conditions adopted in their work; in particular, they showed that for their equation of state, high levels of dissipation (approaching the bound in equation 10) were only realized in cases with rigid walls (as employed in CB17), and not in those with periodic boundary conditions.

Together, these prior results demonstrate that different values of the total dissipative heating are possible in stratified convection. A central aim of this paper is to provide constraints on how much dissipation actually occurs, for the astrophysically relevant case of an ideal gas with rotation.

2 METHODOLOGY

2.1 Model setup

We model a layer of fluid contained between impermeable, free-slip boundaries at $z = 0$ and d and assume that the horizontal boundaries are periodic. Our coordinate system is such that the horizontal coordinates, x and y, correspond to longitudinal and latitudinal directions, respectively, and the vertical coordinate, z,

corresponds to the radial axis. In the majority of our simulations, we retain all three components of velocity but assume all variables are independent of x, so that those simulations are 2D (however, for a few cases in Section 5.5, we relax this constraint and consider the fully 3D case). Gravity acts in the negative z-direction. To drive convection, we impose a flux F at the bottom boundary and fix entropy at the top. Note that for our 2D simulations, F has units of energy per time per length (rather than per area, as in the 3D cases) and F is related to luminosity, L, by $F = L/A$ where, in 2D cases, A is the horizontal box length and in 3D cases A is the horizontal cross-sectional area.

To investigate the effects of rotation on such a convective layer we consider a tilted f-plane, where the rotation vector takes the form $\Omega = (0, \Omega\cos\alpha, \Omega\sin\alpha)$ where Ω is the rotation rate, and α is the latitude. We conducted cases at $\alpha = 90°$ and $45°$; for clarity, in almost all of our discussion below, we focus on cases at $\alpha = 90°$, which corresponds to a vertical rotation vector, aligned with gravity and representative of polar latitudes on a spherical body.

To allow for the effects of a density stratification, we use the anelastic equation set under the Lantz–Braginsky–Roberts approximation (Lantz 1992; Braginsky & Roberts 1995). This is expected to be valid when the flows are sufficiently subsonic and the stratification is nearly adiabatic. We diffuse entropy instead of temperature (see discussions in e.g. Lecoanet et al. 2014). We also consider only the hydrodynamical problem, so there is no Lorentz force and all dissipation is viscous.

The governing equations (in dimensionless form) are as follows:

$$\frac{\partial \boldsymbol{u}}{\partial t} + (\boldsymbol{u} \cdot \nabla)\boldsymbol{u}$$
$$= -\nabla\left(\frac{p}{\bar{\rho}}\right) + \frac{Ra_F}{Pr}\hat{s}\hat{\boldsymbol{e}}_z - Ta^{1/2}\Omega \times \boldsymbol{u} + \frac{1}{\bar{\rho}}\frac{\partial}{\partial x_j}\tau_{ij}, \tag{12}$$

$$\nabla \cdot (\bar{\rho}\boldsymbol{u}) = 0, \tag{13}$$

$$Pr\,\bar{\rho}\bar{T}\left(\frac{\partial s}{\partial t} + (\boldsymbol{u}\cdot\nabla)\,s\right) = \nabla\cdot(\bar{\rho}\bar{T}\nabla s) + \frac{Pr^2\theta}{Ra_F}\tau_{ij}\frac{\partial u_i}{\partial x_j}, \tag{14}$$

where $\boldsymbol{u} = (u, v, w)$ is the fluid velocity, s is the specific entropy, p is the pressure, $\bar{\rho}$ and $\bar{T}$ are the reference state density and temperature, respectively (defined in 17), and

$$\tau_{ij} = \bar{\rho}\left(\frac{\partial u_i}{\partial x_j} + \frac{\partial u_j}{\partial x_i} - \frac{2}{3}\delta_{ij}\nabla\cdot\boldsymbol{u}\right). \tag{15}$$

These quantities are all dimensionless and were obtained from their dimensional counterparts using d as the characteristic length-scale, d^2/ν as the characteristic time-scale (where ν is the kinematic viscosity), and ν/d as the characteristic velocity. Specific entropy has characteristic scale $\frac{Fd}{\kappa\rho_0 T_0}$, where ρ_0 and T_0 are the values of the reference state density and temperature at the bottom of the domain, respectively, and κ is the thermal diffusivity. The characteristic scales for p, density, and temperature are $\rho_0\nu^2/d^2$, ρ_0, and T_0, respectively. Luminosity has scale FA, where A has either characteristic scale d in 2D or d^2 in 3D. Equations (12)–(14) contain several dimensionless parameters defined as follows:

$$Pr = \frac{\nu}{\kappa}, \quad Ta = \frac{4\Omega^2 d4}{\nu^2}, \quad Ra_F = \frac{gd4F}{\nu\kappa^2\rho_0 c_p T_0}, \quad \theta = \frac{gd}{c_p T_0}, \tag{16}$$

where c_p is the specific heat capacity at constant pressure and g is the acceleration due to gravity. In this work, we take ν, κ, c_p, and g to be constant (i.e. they do not vary with depth). Pr is the Prandtl number

and is taken to be unity throughout this study. *Ta* is the usual Taylor number (quantifying Coriolis forces relative to viscous effects) and Ra_F is a flux-based Rayleigh number. Alongside Ra_F, it will also be useful to consider the traditional Rayleigh number defined as $Ra = \frac{gd^3 \delta s}{\kappa \nu}$, where Δs is the entropy difference across the layer. *Ta* and Ra_F will be varied to examine solutions at different rotation rates and at different levels of convective driving.

The reference state is taken to be a time-independent, hydrostatic, ideal gas given by

$$\bar{T} = (1 - \theta z), \quad \bar{\rho} = (1 - \theta z)^m, \tag{17}$$

where $m = \frac{3}{2}$ is the polytropic index.

We will refer to the number of density scale heights across our layer, N_ρ, to quantify the degree of stratification. This is defined as

$$N_\rho = \ln \frac{\bar{\rho}_0}{\bar{\rho}_{\text{top}}} = -m \ln (1 - \theta). \tag{18}$$

In dimensionless terms the boundary conditions amount to enforcing $\frac{\partial s}{\partial z} = -1$ at $z = 0$ and $s = 0$ at $z = 1$. The impermeable and stress-free boundary conditions become, respectively, $w = 0$ and $\frac{\partial v}{\partial z} = 0$ on $z = 0, 1$ (for the 3D simulations in Section 5.5, we also have $\frac{\partial u}{\partial z} = 0$).

We solve this system using the pseudo-spectral code Dedalus (Burns et al. 2020). Our simulations at low and moderate Ra_F generally use 256 grid points in the horizontal and 128 in the vertical with an aspect ratio of 2 (i.e. the box is twice as wide as it is tall); at higher Ra_F, higher resolutions were required (with up to 640 grid points in the vertical direction), and in a few of the highest resolution cases (at $Ta = 10^{11}$) we have considered an aspect ratio of 1.075 instead. The 3D cases in Section 5.5 have an aspect ratio of 2.

The simulations were initialized either by imposing very small entropy perturbations on a motionless base state, or (for some cases at higher Ra_F) from an evolved state at lower Ra_F.

It is convenient to specify the buoyancy driving in a convective system by reference to the value of Ra_F at which convection first occurs, the critical Rayleigh number Ra_c. To find Ra_c, we constructed an eigenvalue problem (EVP) solver using Dedalus (Burns et al. 2020), from which we obtain a grid of growth rates for a given input range of Ra_F and k_y values, where k_y is the horizontal wavenumber. We then used the open-source Eigentools package (Oishi et al. 2021) to find Ra_c (taking into account only those modes that would fit into the finite computational domain). Rotation and stratification both modify the values of Ra_c (see e.g. Chandrasekhar 1967; Mizerski & Tobias 2011). For the parameters studied here, Ra_c then varies from of the order of 100 (for e.g. cases at $N_\rho = 4$, $Ta = 0$) to nearly 10^8 (for cases at $Ta = 10^{11}$).

3 OVERVIEW OF RESULTING DYNAMICS

The convective flows in this system are influenced by rotation, by stratification, and by the level of buoyancy driving. We have conducted simulations that sample a wide variety of possible states within this multidimensional parameter space. We consider cases ranging from the nearly Boussinesq limit ($N_\rho = 0.2$, with a density contrast from top to bottom of only 1.22) up to stronger stratifications with $N_\rho = 4$ (density contrast of 55). The energy passing through the system is quantified by the flux-based Rayleigh number Ra_F, as defined above; our simulations sample both laminar flows near convective onset (with Ra_F close to Ra_c) and more turbulent states that have $Ra_F \sim 10^6 Ra_c$. The rotation rate in our simulations is quantified by the Taylor number defined above, which varies between $Ta = 10$ and 10^{11}. The Ekman number is also commonly used

Table 1. Input parameters and selected output quantities for sample simulations presented in this paper.

| N_ρ	Ra_F/Ra_c	Ra_c	Ta	Ro_c	α	E	Nu
1.4	3.16×10^1	6.74×10^5	10^8	0.46	$90°$	0.82	8.61
1.4	1.78×10^2	6.74×10^5	10^8	1.09	$90°$	0.92	15.3
1.4	5.62×10^2	6.74×10^5	10^8	1.95	$90°$	0.95	19.6
1.4	10^3	6.74×10^5	10^8	2.60	$90°$	0.98	22.1
1.4	10^4	6.74×10^5	10^8	8.21	$90°$	1.05	35.0

Notes. Indicated are the number of density scale heights across the layer (N_ρ), the supercriticality of the simulation Ra_F/Ra_c, the critical Rayleigh number Ra_c, the Taylor number Ta, the convective Rossby number Ro_c, the latitude α (for rotating cases only), and the output quantities E and Nu. Full machine-readable table available online.

to quantify the influence of rotation relative to viscosity; $Ek = Ta^{-1/2}$, so here varies from 3.16×10^{-1} to 3.16×10^{-6}. We conducted simulations at latitudes of $90°$ and $45°$, but in almost all the figures below have chosen to focus on cases at $90°$ for clarity. (None of the key quantities reported in this paper, or their scalings with Ra_F and Ta, appeared to depend significantly on the choice of latitude.) Table 1 lists the input parameters and key-derived quantities for a small number of these simulations; the full table is available online. At each N_ρ, simulations were performed at a range of logarithmically spaced supercriticalities. For cases performed at a fixed supercriticality (e.g. Figs 3 and 6), they were instead logarithmically spaced in Ta.

Increasing the rotation rate stabilizes the system against convection, increasing the value of Ra_c. Thus, for simulations at constant Ra_F, increasing Ta in isolation would eventually result in a system that no longer convects. In much of our discussions below, we therefore choose to compare simulations at varying Ta but constant supercriticality, Ra_F/Ra_c. We also quantify rotation using $\text{Ro}_c = \sqrt{Ra_F/(Ta Pr)}$ (as in e.g. Hindman, Featherstone & Julien 2020; see also Gilman 1978), which assesses the buoyancy driving relative to the Coriolis force (see Anders et al. 2019 for a discussion of how this relates to other measures of rotation). We sample both rapidly rotating cases (with some having volume-averaged values of $Ro_c < 1$) and ones in which rotation has little dynamical role ($Ro_c \gg 1$).

Many different types of flow are possible within this parameter space. Three illustrative examples can be seen in Fig. 1, which shows the specific entropy s for (top row) a non-rotating case at $Ra_F = 10^4 Ra_c$ with a moderate density stratification ($N_\rho = 1.4$), (middle row) a rotating case ($Ta = 10^8$) with the same stratification but $Ra_F = 56.2 Ra_c \approx 3.8 \times 10^7$, and (bottom row) a rotating case ($Ta = 10^8$) at $Ra_F = 10^4 Ra_c \approx 6.8 \times 10^9$.

In our non-rotating simulations, for which a typical case is shown in the topmost panel of Fig. 1, the convection tends to consist of a small number of convective cells, and to be steady in time. These simple flow patterns persist to surprisingly high values of Ra_F in the setup investigated here (as also seen in Boussinesq simulations with stress-free boundaries in, e.g. Wang et al. 2020); in some other problem formulations (e.g. with fixed entropy or temperature boundary conditions), the flow tends to become visibly turbulent at lower values of Ra (see examples in e.g. Rogers, Glatzmaier & Woosley 2003; Anders & Brown 2017). When rotation is dynamically significant, as shown in the middle panel, the convective patterns tend to align with the axis of rotation in accordance with the Taylor–Proudman theorem. Rotating cases at the same Ta but even higher Ra_F (as shown in the bottom panel), in which the Coriolis force is small relative to
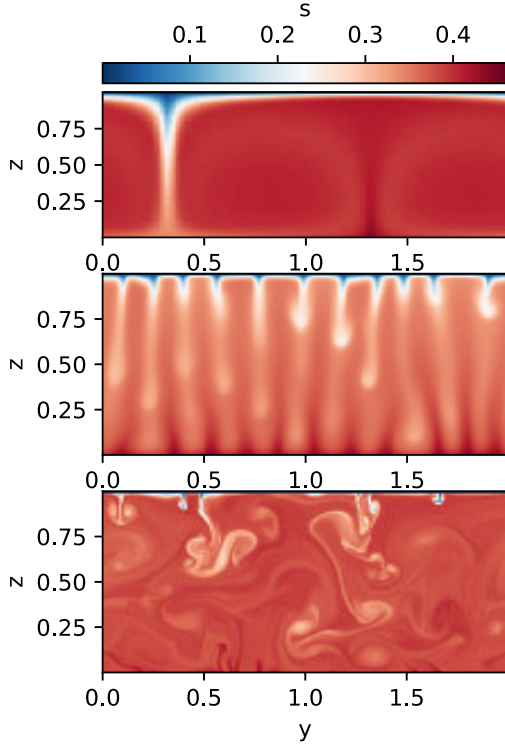
Figure 1. Specific entropy s in three cases sampling different parameter regimes. All cases have $N_\rho = 1.4$; top panel is a non-rotating case ($Ta = 0$) with $Ra_F = 10^4 Ra_c$; middle panel has $Ta = 10^8$ and $Ra_F = 56.2 Ra_c$; bottom panel has $Ta = 10^8$ and $Ra_F = 10^4 Ra_c$.

inertia, exhibit time-dependent flow with structure on many spatial scales.

Most of our simulations behave, qualitatively, like one of the three examples in Fig. 1. The non-rotating simulations (as sampled in the top panel) represent one extreme; the rotating, very high-Ra_F cases (as in the bottom panel) are another. The single-celled case is presumably not realized in any actual star, but serves as a useful limit, showing what can occur when a convective plume travels almost unimpeded from the top to the bottom of the domain; in this limit (as we demonstrate below), most of the dissipation occurs in the bottom boundary layer. The cases with rotation are more realistic, exhibiting flow and dissipation throughout the domain. Below, we explore (for several different stratifications) how the dissipation and dynamics vary in between these extremes, as a function of rotational influence.

4 THE MAGNITUDE AND SPATIAL DISTRIBUTION OF VISCOUS DISSIPATION

4.1 The maximum value of viscous dissipation at high Ra_F

Here, we examine whether the high levels of dissipation found in CB17 are realized in rotating cases as well. We find that, for the levels of stratification examined here, the total amount of dissipative heating in the rotating simulations appears to approach a similar upper bound to that realized in non-rotating calculations. The models here were conducted with a different aspect ratio than in CB17 (here the horizontal layer size is twice its depth, whereas in CB17 they were equal) and different boundary conditions (here periodic, impermeable in CB17), so we also indirectly show that these results
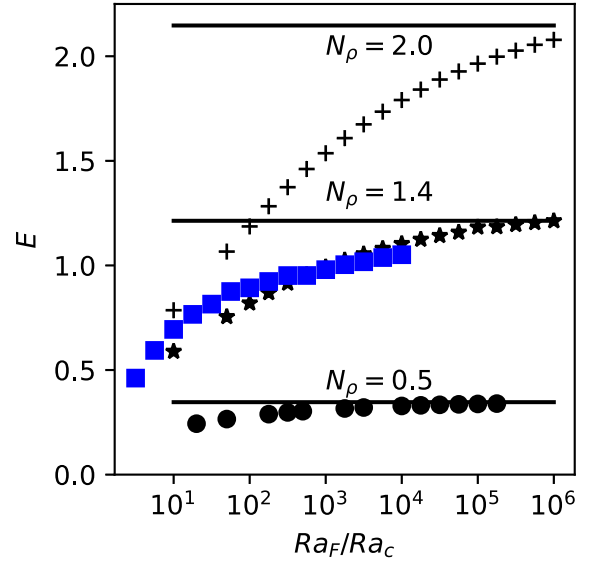
Figure 2. Calculated values of E at a range of stratifications and supercriticalities for sample non-rotating (black) and rotating cases (blue). Values of $N_\rho = 0.5$ (circles), 1.4 (stars and blue squares), and 2.0 (pluses) are used. The horizontal black lines represent the value of equation (10) for each value of N_ρ. The rotating cases are at latitude 90° with $Ta = 10^8$. Note that due to the effect of rotation on the critical Rayleigh number, the rotating cases have considerably larger values of Ra_F for a given stratification.

are, for an ideal gas equation of state, not directly dependent on these factors.

Fig. 2 shows E for a representative selection of cases at different Ra_F and Ta, for three different stratifications. For our non-dimensional setup, E is given by

$$E = \frac{Pr^2\theta}{A Ra_F} \int_V \tau_{ij} \frac{\partial u_i}{\partial x_j} \, dV. \tag{19}$$

Recall that A is now non-dimensional, and so for our 2D simulations it is equal to the aspect ratio of the layer, while for the 3D cases, A is equal to the aspect ratio squared. The horizontal lines in Fig. 2 show the value of equation (10) at each value of N_ρ. At high enough supercriticalities, both the rotating and non-rotating cases appear to approach this limiting value, which is dependent on the layer depth and stratification but independent of Ra_F (and likewise also independent of viscosity or diffusivity). We have found no cases that exceed this value, but (because it is only an empirical bound) cannot rule out the possibility that it would be exceeded at higher Ra_F or for other parameter regimes. We have displayed example cases at $Ta = 10^8$; our cases at $Ta = 10^{11}$ and latitude 45° exhibit identical behaviour. Both the rotating and non-rotating cases shown here exceed $E = 1$ (i.e. the total integrated dissipative heating exceeds the imposed luminosity) at high enough Ra_F. However, we cannot rule out different asymptotic values of E for the rotating and non-rotating cases, as discussed in more detail below.

It is clear from Fig. 2 that the empirical bound on dissipative heating given by equation (10) is approached only for sufficiently high Ra_F/Ra_c, and that the value of Ra_F/Ra_c needed to reach the upper bound is different for each N_ρ. The largest N_ρ cases have not quite reached the asymptotic upper limit as they have not been performed at a high enough supercriticality.

A complementary view but instead focused on the influence of rotation is provided by Fig. 3, which shows E for a selection of cases
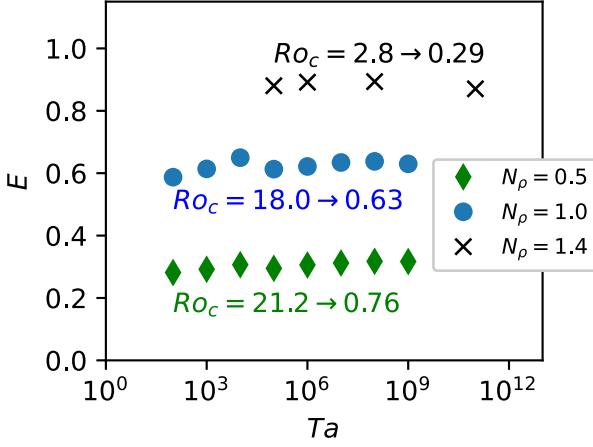
Figure 3. The values of E for a range of rotation rates. All cases have a fixed supercriticality of $Ra_F/Ra_c = 10^2$; we consider stratifications of $N_\rho = 0.5$, 1, and 1.4. The labels show the range of the convective Rossby number Ro_c for increasing values of Ta at each stratification. All simulations shown are at latitude $90°$, except for the point at $Ta = 10^{11}$ which is at $45°$.

at fixed supercriticality (here $Ra_F = 10^2 Ra_c$) and three different N_ρ but varying Ta (i.e. with varying rotational influence relative to viscous effects). In the regime probed here, it is clear that the presence of rotation does not greatly alter the volume-integrated magnitude of viscous dissipation despite significant changes in the dynamics.

Note that because rotation stabilizes the system against convection, the high-Ta cases shown here have appreciably higher Ra_F than non-rotating cases at the same supercriticality. We have that $Ra_c \propto Ta^{2/3}$ (Chandrasekhar 1967), so for example, cases at $Ta = 10^{11}$ require Ra_F about 10^7 times higher than non-rotating equivalents to reach the same supercriticality. The convective flow fields in the rotating cases are, at equivalent Ra_F/Ra_c, more complex than in the non-rotating cases, but they eventually asymptote to similar levels of viscous dissipation. Further, the cases shown here span a range of convective Rossby numbers, from $Ro_c \approx 22$ in the lowest Ta cases to ≈ 0.3 at $Ta = 10^{11}$, and so sample both cases in which rotation plays little dynamical role (with $Ro_c \gg 1$) and those in which it is more significant ($Ro_c < 1$).

4.2 Entropy generation by dissipation and conduction

In the previous section, we suggested that in both rotating and non-rotating cases, the total viscous dissipation at first increases with increased buoyancy driving (higher Ra_F) and then plateaus at or below a fixed value (10) that depends on the layer height and stratification but is independent of the rotation rate or diffusivities. Here, we begin to explore how this arises. To do so, we consider entropy generation by conduction and dissipation at varying Ra_F.

In a steady state, the energy entering the convection zone at the bottom boundary (by conduction) must equal the energy leaving at the top boundary (also by conduction). The top boundary is at a lower temperature than the bottom one, so the conductive entropy flux out the top is larger than the entropy flux entering the domain; the difference must be made up by entropy generation within the domain, associated with either conduction or viscous dissipation. For our simulations (employing entropy diffusion and without magnetic
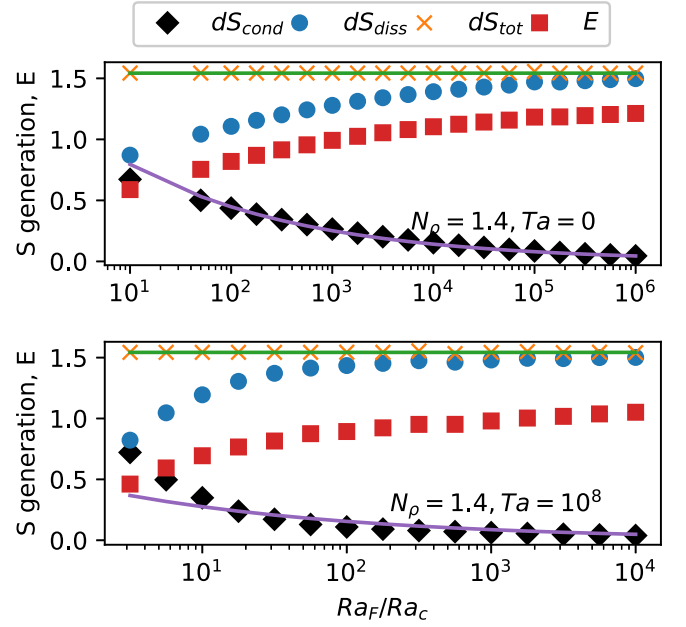
Figure 4. Entropy generation terms as given in equation (21), for example, non-rotating (top panel) and rotating (bottom panel) simulations at $N_\rho = 1.4$ and varying Ra_F. Shown for each case is the entropy production due to conduction (dS_{cond}) and viscous dissipation (dS_{diss}), together with their sum (dS_{tot}). Also shown (as horizontal green line) is the entropy mismatch dS_{out-in} for each case; in all cases, the sum of dS_{cond} and dS_{diss} matches dS_{out-in}. For comparison, we also plot the value of E for each case, and indicative $Ra_F^{-1/4}$ scaling over the dS_{cond} values; see the text for discussion of this scaling.

fields), this implies that

$$0 = \int_V \left[\nabla \cdot \left(\frac{\bar{\rho}\bar{T}\nabla s}{\bar{T}} \right) + \frac{\bar{\rho}\bar{T}\nabla s \cdot \nabla \bar{T}}{\bar{T}^2} + \frac{Pr^2\theta}{Ra_F} \frac{1}{\bar{T}} \tau_{ij} \frac{\partial u_i}{\partial x_j} \right] dV,$$
(20)

and so

$$\underbrace{A(e^{N_\rho/m} - 1)}_{dS_{out-in}} = \underbrace{\int_V \frac{\bar{\rho}\bar{T}\nabla s \cdot \nabla \bar{T}}{\bar{T}^2} dV}_{dS_{cond}} + \underbrace{\frac{Pr^2\theta}{Ra_F} \int_V \frac{1}{\bar{T}} \tau_{ij} \frac{\partial u_i}{\partial x_j} dV}_{dS_{diss}},$$
(21)

which follows from equation (14) after integration (using the divergence theorem and the constraint of mass conservation). We have also used $\left[-\frac{\bar{\rho}\bar{T}\frac{\partial s}{\partial z}}{\bar{T}} \right]_{z=0}^{z=1} = e^{N_\rho/m} - 1$. For reference, we note that the dimensional equivalent of equation (21), retaining entropy diffusion, would be

$$L \left(\frac{1}{T_{top}} - \frac{1}{T_0} \right) = \int_V \frac{\kappa \bar{\rho}\bar{T}\nabla s \cdot \nabla \bar{T}}{\bar{T}^2} dV + \int_V \frac{1}{\bar{T}} \tau_{ij} \frac{\partial u_i}{\partial x_j} dV,$$
(22)

and the dimensional equivalent for temperature diffusion, and including magnetism and internal heating, is equation (8).

In Fig. 4, we examine the terms in (21) for a series of calculations at varying Ra_F, N_ρ, and Ta. In all cases, the sum of the terms, on the right hand side of equation (21) (dS_{cond} and dS_{diss}), correctly matches dS_{out-in}, the mismatch between the entropy flux at the top and bottom boundaries. As Ra_F increases, the relative contributions of conduction (dS_{cond}) and dissipation (dS_{diss}) change: at low Ra_F, both processes contribute to the entropy balance, whereas at high enough Ra_F there is negligible entropy generation by conduction within the bulk.

In the non-rotating cases, the bulk becomes nearly isentropic at high Ra_F, so that the conductive entropy generation term dS_{cond} is then confined mainly to thin thermal boundary layers whose width (discussed in Section 5.4) decreases with Ra_F. Thus dS_{cond} scales roughly with the width of these boundary layers; as shown in Section 5.4, the largest (top) boundary layer width scales as $Ra_F^{-1/4}$ in our simulations. We have therefore plotted a corresponding $Ra_F^{-1/4}$ dependence in Fig. 4 to guide the eye; in the non-rotating cases dS_{cond} appears to follow this trend reasonably well. (The line is not a fit; it is chosen to pass through the fourth data point for illustrative purposes.) The behaviour in the rotating cases is more complicated, as discussed below, partly because, in these cases, the entropy gradient (and hence also dS_{cond}) is non-zero in the bulk.

These trends are linked to the values of E explored above. We have overplotted the measured values of E at each Ra_F in Fig. 4. The simulations with the highest E values are those in which entropy generation by conduction is negligible; further, in non-rotating cases, the Ra_F-dependence of E is well matched by the Ra_F-dependence of dS_{diss} (which, in turn, is linked to the width of the thermal boundary layers as noted above).

These results also help us understand why simulations must be run at much higher Ra_F to reach the 'dissipative asymptote' when the stratification is strong (i.e. at high N_ρ). The purely conductive state has

$$dS_{cond} = dS_{out-in} = A(e^{N_\rho/m} - 1), \quad (23)$$

which increases with increasing N_ρ.

However, knowledge of dS_{diss} alone is not sufficient to determine the actual *value* of E at each Ra_F. In the limit of high Ra_F, when dS_{cond} is negligible, we know that

$$dS_{diss} = \frac{Pr^2\theta}{Ra_F} \int_V \frac{1}{\bar{T}} \tau_{ij} \frac{\partial u_i}{\partial x_j} dV = dS_{out-in} = A(e^{N_\rho/m} - 1). \quad (24)$$

Meanwhile, recall that $E = \frac{Pr^2\theta}{Ra_F A} \int_V \tau_{ij} \frac{\partial u_i}{\partial x_j} dV$, so the highest possible E value consistent with the known dS_{diss} occurs if all the dissipation is at the highest possible temperature. As noted in Section 1, the firm upper bound of HMW75 corresponds to this limit. More generally, the value of E actually attained depends on both the *magnitude* of the dissipative entropy generation term dS_{diss} and on *where it occurs*. For example, if $-\tau_{ij}\partial u_i/\partial x_j \equiv Q_0$ were constant throughout the domain, we would have $E = -\frac{Pr^2\theta}{Ra_F} Q_0$, with $dS_{diss} = -\frac{Pr^2\theta}{Ra_F} Q_0 A \int_0^1 (dz/\bar{T})$, which (upon substituting for $\bar{T}$ and integrating) gives

$$dS_{diss} = -\frac{Pr^2}{Ra_F} \frac{Q_0 A N_\rho}{m}. \quad (25)$$

Equating this to dS_{out-in} allows us to solve for Q_0 in this limit. This, in turn, allows calculation of E for this situation,

$$E = \frac{m\theta}{N_\rho}(e^{N_\rho/m} - 1), \quad (26)$$

which reduces to $E \approx \theta = 1 - e^{-N_\rho/m}$, if N_ρ is small.

Our rotating cases at very high Ra_F, which have $Ro_c > 1$ and exhibit intricate flow fields, exhibit E close to the value predicted by equation (26), though they slightly exceed it at the highest Ra_F we have probed. They always remain below the limit of equation (10). For example, at $N_\rho = 1.4$, equation (26) yields $E \approx 1.00$, whereas equation (10) gives $E \approx 1.21$ and equation (9) yields $E \approx 1.54$; our highest Ra_F, $Ta = 10^8$ simulation at that stratification, shown in Fig. 2, has $E \approx 1.05$. In comparison, many of our non-rotating simulations (which have simpler flow fields) exhibit values of E that exceed

equation (26), the predicted value of E for uniform dissipation. For example, at $N_\rho = 2$, equation (26) would yield $E \approx 1.54$, whereas our highest Ra_F non-rotating simulations at that stratification have $E \approx 2.08$. This is closer to, but does not exceed, the limit described by equation (10), which for the same stratification is 2.15. (We have found no cases that exceed the empirical bound in equation 10, which is always tighter than the firm bound of equation 9. For example, at $N_\rho = 2$, the latter is 2.8, which is significantly larger than in our highest Ra_F cases.)

If the dissipation were uniformly distributed throughout the domain, equation (26) would provide a useful bound on E. Some of our simulations exceed this bound, so evidently, in at least these cases, the dissipation is *not* uniform: a disproportionate amount must occur at higher temperatures, allowing E to be higher than suggested by equation (26) while still satisfying the entropy constraint that $dS_{diss} = dS_{out-in}$. In the following section, we explore how and when this occurs.

### 4.3 The spatial distribution of dissipation

Here, we determine where the dissipation occurs in our simulations. We show – in particular by examination of a 'dissipation half-height' (defined to be the height by which half of the dissipation occurs) – that the non-rotating cases at high Ra_F which approach the CB17 upper bound correspond to situations in which much of the dissipation occurs close to the bottom of the domain and there is negligible entropy generation by conduction in the bulk. In rotating cases, the dissipation is more uniformly distributed throughout the interior.

We begin by defining $L_{diss}(z) = A \int_0^z Q_{diss} dz'$, where Q_{diss} is the horizontal average of $-\frac{Pr^2\theta}{Ra_F}\tau_{ij}\partial u_i/\partial x_j$ (the local dissipative heating). Here, L_{diss} represents the total dissipative heating up to height z, so if the heating were uniformly distributed throughout the interior (with Q_{diss} a constant) L_{diss}/L would be a linear function of height, increasing from zero at the lower boundary to $-E$ at the top. Qualitatively, we find that $L_{diss}(z)$ is close to linear for our rotating cases; the dissipative heating is nearly uniform throughout the domain. In our non-rotating cases, by contrast, much of the dissipation occurs near the lower boundary. Examples, and a discussion of how these are linked to the buoyancy work and to the dynamics, can be found in Section 5.1.

A simple, quantitative assessment of the sites where dissipation occurs is provided by Fig. 5, which shows what we call the 'dissipation half-height' z_{diss} in a range of cases. We define this as the location at which L_{diss} reaches *half* its maximum (absolute) value. That is

$$\frac{|L_{diss}(z_{diss})|}{L} = \int_0^{z_{diss}} Q_{diss} dz = \frac{E}{2}. \quad (27)$$

If the convection and dissipation were uniform throughout the domain, z_{diss} would be 0.5; meanwhile, if the dissipation occurs predominantly at the lower boundary, z_{diss} will tend towards the width of the lower dynamical boundary layer. In both the rotating and non-rotating cases, z_{diss} declines at first with increasing supercriticality: more and more of the dissipation occurs close to the bottom boundary. In the non-rotating cases it appears to level out (i.e. is approximately constant) at high enough Ra_F. In the non-rotating cases studied here – that is, in 2D and at $Pr = 1$ specifically – at high enough Ra_F the flow consists of a steady cell of convection. Thus, there is dissipation around the single downflow plume, and in the top and bottom dynamical boundary layers, but very little elsewhere in the bulk. In this limit, z_{diss} is related to the point at which the flow is bent
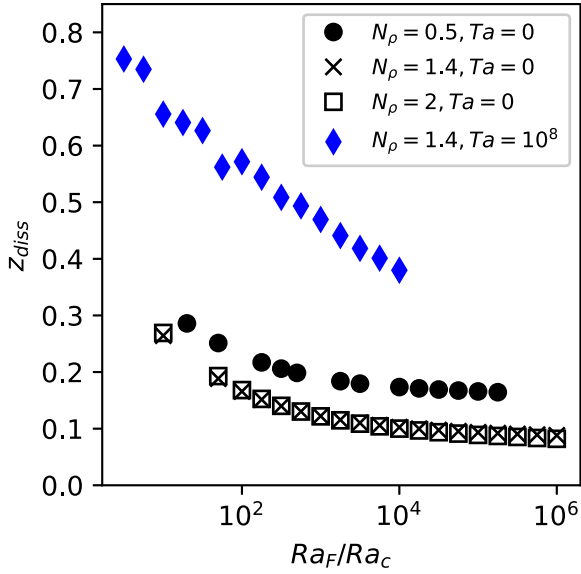
Figure 5. Values of z_{diss} for a range of non-rotating and rotating simulations at a range of stratifications, N_ρ. All rotating cases shown are at latitude 90°.
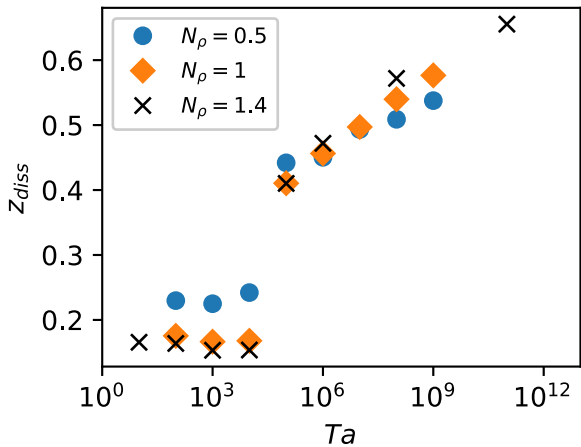
Figure 6. Values of z_{diss} for a range of simulations at fixed supercriticality, $Ra_F = 10^2 Ra_c$ for stratifications of $N_\rho = 0.5$, 1.0, and 1.4 and a range of Ta. All cases shown are at latitude 90°, except for the point at $Ta = 10^{11}$ which is at 45°.

from the vertical towards the horizontal, and this occurs progressively nearer the lower boundary at moderate Ra_F.

In the rotating cases, the dissipation is more uniformly distributed throughout the domain, so z_{diss} is (at any given Ra_F) higher than in the non-rotating cases. However, z_{diss} still declines as Ra_F increases. Note that at fixed Ta, as sampled here, increasing Ra_F/Ra_c implies *decreasing* rotational influence on the dynamics, so that the cases at high Ra_F and lower z_{diss} have a higher Rossby number.

A complementary view is provided by Fig. 6, which examines the value of z_{diss} in a series of cases at the same supercriticality $Ra_F = 10^2 Ra_c$ but varying Ta. Here, we find that z_{diss} increases with increasing Ta (i.e. with increasing rotation rate). That is, stronger rotation leads to more of the dissipation occurring in the bulk of the domain, far from the lower boundary. There is a fairly sharp transition between a 'low-z_{diss}' state at low Ta (high Rossby number) to a 'high-z_{diss}' state for higher Ta; beyond this, z_{diss} increases slowly with increasing Ta (i.e. with increasing rotational influence). This

transition is connected to the transition from single-cell states (as achieved in non-rotating cases or at very low Ta) to much more intricate, time-dependent flows realized at higher Ta and Ra_F.

These changes in the spatial distribution of the dissipation must be linked to changes in the flow field. Since the local dissipative heating is related to the stress tensor $\tau_{ij}\partial u_i/\partial x_j$, changes in either the magnitude of u, or in the characteristic length-scales present in the flow, will affect Q_{diss}. Both these quantities are expected to depend on rotation rate (e.g. Aurnou, Horn & Julien 2020; Currie et al. 2020; Nicoski, O'Connor & Calkins 2023), so it is natural that the dissipation exhibits some dependence on this as well. However, L_{diss} must obey the bounds described in Section 4.2 at all rotation rates.

Flows in 3D, or in real stars, are bound to exhibit more complexity at all rotation rates, and so we do not expect the numerical values of z_{diss} (for example) to be the same in such cases. Equivalently, the relative proportion of bulk and boundary dissipation might well be different. (In the context of stellar convection, with no impermeable boundaries, the equivalent of 'boundary' dissipation might be convective plumes that are dissipated only when they reach adjacent stably stratified layers.) The extremely low-z_{diss} states seen here at low Ta are also unlikely to be realized in any real star, since they occur only for single-cell flows with little bulk dissipation. However, we expect that both the thermodynamic bounds discussed here, and the general trend towards increasing dissipation in the bulk at higher rotation rates, may be robust.

5 LINKS BETWEEN DYNAMICS, HEAT TRANSPORT, AND DISSIPATION

In a steady state, dissipation and dynamics are linked, so insight into either one yields constraints on the other. Here, we briefly explore how systematic variations in the governing parameters of this problem (namely Ra_F, Ta, and N_ρ) lead to changes in the energy transport and in the flow fields, and we explore how these are related to changes in the magnitude and spatial distribution of the dissipation. Our discussion here is also intended to help place our work in context with a large body of previous research on heat transport in both non-rotating and rotating convection.

In stellar astrophysics, the main purpose of a convective theory is to provide estimates of the entropy gradient needed to carry a certain luminosity outwards (e.g. Gough & Weiss 1976). For example, in standard stellar evolution theory, the radius of a star depends on its specific entropy, and how this varies with depth (see e.g. discussions in Ireland & Browning 2018). There is also substantial astrophysical interest in properties of the flow itself – for example, its magnitude at each depth – since these, in turn, will affect mixing, the transport of heat and angular momentum, and the generation of magnetic fields. Hence, we focus our discussions here on the heat transport, on the related question of how entropy varies with height in our simulations, and on the magnitude of the flows themselves. In Section 5.2, we demonstrate that a quantity of particular interest, the kinetic energy flux, can be estimated given knowledge of the dissipative heating.

5.1 Energy balances and transport terms

In this section, we begin to quantify the links between energy transport in our simulations, and where the dissipation occurs.

One view of this is provided by Fig. 7, which assesses the energy transport in two example calculations. The top panels consider a non-rotating case at $N_\rho = 4$ and $Ra_F = 10^5 Ra_c$; the bottom
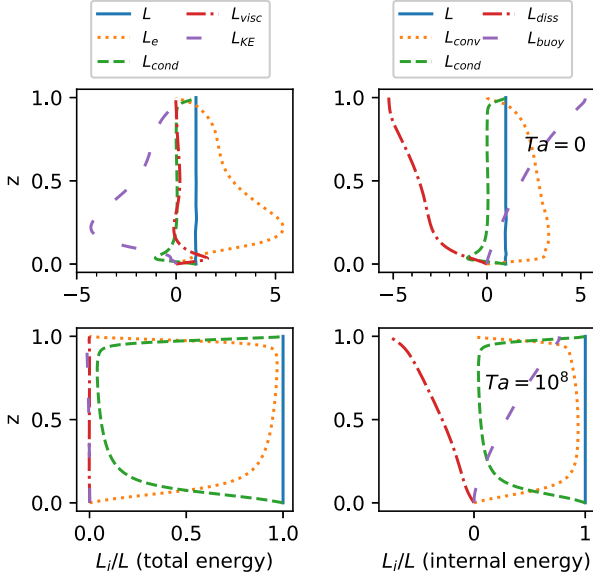
Figure 7. Fluxes of energy provided by different transport terms in the total energy equation (left panels) and internal energy equation (right panels), for example, 2D cases at (top panel) $N_\rho = 4$ without rotation and (bottom panel) $N_\rho = 1.4$ with rotation ($Ta = 10^8$).

ones are for a rotating case with $N_\rho = 1.4$, $Ra_F = 17.8Ra_c$, and $Ta = 10^8$.

We assess the transport in two complementary ways. The right panels show the terms arising in the following equation, which arises after integration and manipulation of the total energy equation (equation 3):

$$L = FA = \underbrace{Pr \int_{S_z} \bar{\rho}\bar{T}sw\,\mathrm{d}S}_{L_{conv}=AF_{conv}} + \underbrace{\int_{S_z} -\bar{\rho}\bar{T}\frac{\partial s}{\partial z}\,\mathrm{d}S}_{L_{cond}=AF_{cond}}$$

$$+ \underbrace{Pr \int_{V_z} -s\bar{\rho}(\boldsymbol{u}\cdot\nabla)\bar{T}\,\mathrm{d}V}_{L_{buoy}=A\int_0^z Q_{buoy}\mathrm{d}z'} + \underbrace{\frac{Pr^2\theta}{Ra_F}\int_{V_z} -\tau_{ij}\frac{\partial u_i}{\partial x_j}\,\mathrm{d}V}_{L_{diss}=A\int_0^z Q_{diss}\mathrm{d}z'}, \quad (28)$$

where the volume integrals are over the volume enclosed between $z' = 0$ and z and the surface integrals are over the bounding surfaces of that volume. The convective heat flux (F_{conv}) is defined by the first term; the conductive heat flux (F_{cond}) by the second; the third and fourth terms define heating and cooling terms (Q_{diss} and Q_{buoy}) arising from the viscous dissipation and from work done against the background stratification, respectively (as also discussed in Section 4.3). As noted in CB17, these latter two terms must balance when integrated over the entire layer, but they do not have to balance at each depth.

The left panels instead arise from considering the total energy balance (i.e. including kinetic energy as well as internal), which in a steady state may be written as (see e.g. Viallet et al. 2013)

$$L = FA = \underbrace{\int_{S_z} Pr\bar{\rho}sw + \frac{Pr^2\theta}{Ra_F}\bar{\rho}w\tilde{p}\,\mathrm{d}S}_{L_e=AF_e} + \underbrace{\int_{S_z} -\bar{\rho}\bar{T}\frac{\partial s}{\partial z}\,\mathrm{d}S}_{L_{cond}=AF_{cond}}$$

$$+ \underbrace{\frac{Pr^2\theta}{Ra_F}\int_{S_z} \frac{1}{2}\bar{\rho}|u|^2|w\,\mathrm{d}S}_{L_{KE}=AF_{KE}} + \underbrace{\frac{Pr^2\theta}{Ra_F}\int_{S_z} -(\tau_{ij}u_i)\cdot\hat{\mathbf{e}}_\mathbf{z}\,\mathrm{d}S}_{L_{visc}=AF_{visc}}, \quad (29)$$

defining the enthalpy flux (F_e), the kinetic energy flux (F_{KE}), and the viscous flux (F_{visc}). It is common for global-scale simulations of stellar convection to decompose the transport in this way (e.g. Browning, Brun & Toomre 2004; Featherstone & Hindman 2016). In the notation here, and in Fig. 7, positive fluxes are defined to be vertically upwards.

Whether considering the total or internal energy equations, in a steady state the sum of the transport terms must equal L, the total luminosity, which is constant throughout the layer. The sum of the transport terms is indicated in Fig. 7 by a solid line, which is indeed constant with depth in all the sampled cases. In general, we use $L(z)$ as a gauge of whether a given simulation has been evolved for a long enough time, and averaged over long enough intervals, for the results to be time-independent. We evolved all cases in this paper long enough for $L(z)$ to vary by less than one per cent across the layer, and for other aspects of the dynamics (e.g. the kinetic energy evolution) to equilibrate as well. This means that the simulations were evolved for typically tens of viscous diffusion times, and averaged over intervals ranging from 0.1 to several diffusion times.

The energy transport differs substantially in our non-rotating and rotating cases. The top row in Fig. 7 is an example of what can occur in non-rotating, stratified cases: Here (left panel), the enthalpy flux exceeds the total flux in magnitude; this excess is compensated largely by a negative (inward-directed) kinetic energy flux. Broadly similar transport has been observed in simulations of stratified convection for decades (see e.g. Hurlburt, Toomre & Massaguer 1984 in 2D; Stein & Nordlund 1989; Featherstone & Hindman 2016). Transport by conduction is small throughout the layer, outside of narrow boundary layers.

By contrast, in the example rotating case (bottom row) the kinetic energy flux is negligible; the enthalpy flux is approximately equal to the total luminosity, with conductive transport small outside the boundary layers. At this particular Ra_F, the conductive boundary layers are still relatively large, and there is evident asymmetry between the top boundary layer and the bottom one (which have different widths).

The connection between this transport and the viscous dissipation is made clearer by comparison to the right panels of Fig. 7, which considers the internal energy decomposition for the same cases. In all cases, the buoyancy work is fairly evenly distributed throughout the domain – that is, outside of the bottom boundary layer L_{buoy} rises linearly towards the top domain. The rotating case has fairly uniform dissipative heating, with L_{diss} also nearly linear. But in the non-rotating case, the dissipative heating L_{diss} is non-uniform: More of the dissipation is occurring near the bottom boundary. At the upper boundary, both L_{buoy}/L and L_{diss}/L must approach $+/-E$, respectively, and they do so in both cases; what differs in the rotating and non-rotating simulations is the spatial distribution of L_{diss}. The convective luminosity L_{conv}, as defined and plotted here, is often larger than the total luminosity in the non-rotating cases, in accord with the fact that L_{diss} is greater in magnitude than L_{buoy} throughout much of the convection zone. In the rotating cases, where there is approximate local balance (as well as an exact global balance) between the dissipative heating and the 'cooling' by buoyancy work, the convective luminosity is closer to unity.

5.2 Predicting the kinetic energy flux from the viscous dissipation

The transport revealed here differs in some important ways from that envisioned in MLT, and some of these differences are connected to where the viscous dissipation occurs. In this section, we consider

the kinetic energy flux, which is not explicitly included in classical MLT (e.g. Gough & Weiss [1976]) but is a robust feature of stratified convection in stellar environments. Generally, we find that the enthalpy flux exceeds the total luminosity by a considerable amount, and is compensated for by the inward-directed KE flux. However, prior work has not clearly established what sets the amplitude of these fluxes. Might it be possible, for example, for a star like the Sun to have a thousand solar luminosities moving outwards in the enthalpy flux, and 999 moving inwards via the KE flux? In this section, we show that knowledge of the viscous dissipation can answer this question, and more generally provide constraints on the magnitude of the kinetic energy flux.

Following CB17, we define $F_{other} = \int_0^z (Q_{buoy} + Q_{diss}) dz'$, so that if conduction is negligible the total flux $F \approx F_{conv} + F_{other}$. Equivalently, $F_{other} = F_p + F_{KE} + F_{visc}$, where $F_p = \frac{1}{A} \int_{S_z} wp \, dS$. Hence, F_{other} is equivalent to the steady-state transport associated with processes other than the convective flux as defined above. Outside of the boundary layers, prior work has found that F_{KE} is generally larger in magnitude than F_p or F_{visc} (e.g. Viallet et al. [2013]), so that in the bulk $F_{other} \approx F_{KE}$.

If the local dissipation and buoyancy work terms *do* balance at each depth, then F_{other} is zero. This, in turn, implies negligible kinetic energy flux. This is approximately the state attained in some of our rotating cases: There, both L_{diss} and L_{buoy} are linear in z, and of similar magnitude, so that $F_{other} \ll F$.

In our non-rotating 2D cases, by contrast, the concentration of much of the dissipative heating near the bottom boundary implies a substantial mismatch between dissipative heating and buoyancy work throughout much of the bulk, so F_{other} is no longer negligible. This, in turn, requires a substantial kinetic energy flux.

We can use these ideas to place simple bounds on the magnitude of the kinetic energy flux. Consider the extreme case in which *none* of the viscous dissipation occurs in the bulk (i.e. it is all in a comparatively narrow bottom boundary layer). At some depth just *above* this boundary layer, nearly all the integrated viscous heating will have occurred, but very little of the integrated work will have; in the notation employed here, L_{buoy}/L will be close to zero, while L_{diss}/L will be nearly equal to its value at the top of the domain. The latter is bounded by $E = d/\hat{H}_T$, as discussed above, so we have $L_{other}/L \approx E$ just above the bottom boundary. Hence, if the 'other' transport is dominated by the KE flux (rather than L_p or L_{visc}) we expect the maximum absolute value of L_{KE}/L to be bounded by the value of E at each stratification.

We examine this prediction in Fig. [8], which shows the maximum absolute value of the kinetic energy flux in a series of calculations at varying N_ρ at high supercriticality ($Ra_F \geq 10^4 Ra_c$), along with the limiting value of E given by equation ([10]) and the actual value of E attained in the simulation. For cases at N_ρ of two or less, the measured E values adhere closely to the limiting value (indicated by the black line); at the highest N_ρ, the measured values are lower than the theory. The KE flux closely tracks the measured value of E at each stratification (lying slightly below it), in keeping with the simple model described above.

These results suggest that at high enough Ra_F the *maximum possible* amplitude of the kinetic energy flux may be estimated simply by calculating $E = d/\hat{H}_T$ (equation [10]). Our non-rotating cases, which consist of simple unicellular flows, actually approach this limit. However, (as noted above) in rotating cases, the dissipative heating more nearly balances the buoyancy work at each height, leading to significantly smaller kinetic energy fluxes. Likewise, more complex flows (as likely realized at higher Ra_F in real stars) likely lead to smaller KE fluxes as well. We speculate, though, that the
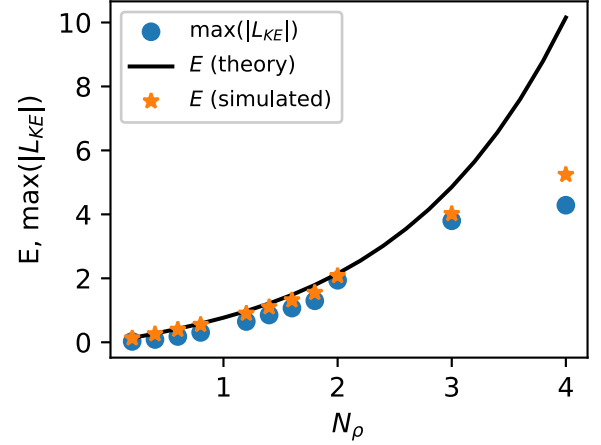
Figure 8. Comparison between KE flux amplitudes in theory and simulation. Shown as a solid line is the estimate of equation ([10]) for E in non-rotating convection at very high Ra_F, which we argue in the text provides a bound on the maximum KE flux amplitude. Also shown are the values of E in sample non-rotating simulations (at high but finite supercriticality) and the maximum absolute values of the KE flux in the same simulations.

limits on the KE flux developed here are unlikely to be *exceeded* by real convective flows. For this to occur, the dissipation and buoyancy work would have to be even more imbalanced than in our single-plume non-rotating cases; for uniform buoyancy work, this would require the dissipation to be concentrated to an even smaller part of the domain than in these simulations.

5.3 Entropy profiles and Nusselt number scalings

In previous sections, we saw that the energy transport in our simulations – and, in particular, the relative contributions of conduction and convection – varied in response to changes in the key controlling parameters N_ρ, Ra_F, and Ta. Here, we explore how these variations arise, and, in particular, how they are linked to the entropy gradients established by the convection.

In our work, entropy is fixed at the upper boundary; at the lower boundary, its gradient is fixed. Recall also that we have assumed that conductive transport is proportional to entropy gradients (rather than temperature gradients). Together, these imply that in the *absence* of convection, we would expect a linear specific entropy profile, extending from $s = 0$ at the top to Δs_{cond} at the bottom. For the models considered here, Δs_{cond} is

$$\Delta s_{cond} = \frac{1}{\theta m}[e^{N_\rho} - 1]. \tag{30}$$

If convection occurs, a smaller total entropy contrast between the top and bottom boundaries, Δs, is required to carry the same imposed F. In our simulations the total Δs, and its variation with height, are functions of N_ρ, Ra_F, and Ta. We assess these for two illustrative cases in Fig. [9], which shows $\langle s \rangle(z)$ (where $\langle \cdot \rangle$ denotes a horizontal average) for both a rotating case (at $Ta = 10^8$ and $Ra_F = 17.8 Ra_c$) and a rotating one (with $Ra_F = 10^4 Ra_c$) at $N_\rho = 1.4$. In both cases, conduction must carry all the energy within some distance of the boundaries, so there are steep entropy gradients at the top and bottom of the domain; the entropy gradient is smaller in the bulk. The total Δs across the layer is similar in the two cases, but its spatial variation is different: In the non-rotating, the interior is nearly isentropic ($\langle s \rangle$ is close to a vertical line), whereas in the rotating case there is a visible, finite slope to $\langle s \rangle$ throughout the bulk.
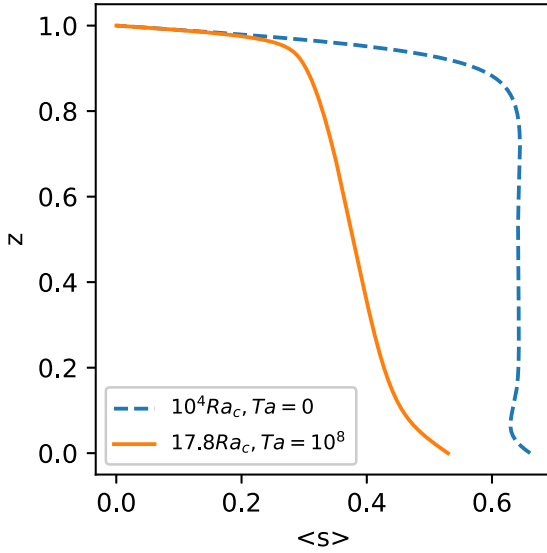
Figure 9. Horizontally averaged specific entropy as a function of depth in two example cases, both at $N_\rho = 1.4$. The solid (orange) line is for a rotating case at $Ta = 10^8$ and the dashed (blue) line is for a non-rotating case ($Ta = 0$).

To analyse these trends quantitatively, we turn to an average measure of the heat transport over the domain (rather than to its spatial variation). In studies of Rayleigh–Bénard convection, it is customary to encapsulate this via the Nusselt number Nu, a dimensionless measure of the heat transport relative to that provided by conduction. There is no universally accepted definition of Nu that makes sense for all boundary conditions, stratifications, and with/without rotation, but sensible definitions have the property that they are large when convection is efficient, and tend to one as the convection vanishes (i.e. as all transport becomes conductive). For the mixed fixed-flux, fixed-entropy boundary conditions here, we choose to adopt

$$Nu = \frac{\Delta s_{\text{cond}}}{\Delta s} \qquad (31)$$

as our definition of Nu. This is a global measure of the efficiency of the convective flow – more efficient convection should have a smaller Δs across the layer, and so a higher Nu – but normalized to the Δs_{cond} that would be required to carry the flux in the absence of convection. This is akin to the definition for Boussinesq convection adopted by, for example, Kazemi, Ostilla-Mónico & Goluskin (2022).

The resulting measures of Nu are plotted for a sample of cases with varying Ra_{F}, N_ρ, and Ta in Fig. 10. We have also overplotted several previously proposed scaling relations, as discussed below. We have chosen here not to normalize each case by Ra_c, primarily because Ra_c varies so much across the simulations sampled here; in general, each 'track' of simulations shown begins with Ra_{F} of the order of 10 times critical at that N_ρ and Ta.

First, consider the non-rotating, weakly stratified cases at $N_\rho = 0.5$. These are well matched by the power-law $Nu \propto Ra_{\text{F}}^{1/4}$, which is obtained if transport within the bulk is entirely by convection, transport within narrow thermal boundary layers is by conduction, and the width of the boundary layers is set by the requirement that they be marginally stable against convection (Malkus 1954). The scaling at higher N_ρ appears to be slightly less steep than this. For comparison, we have overplotted $Nu \propto Ra_{\text{F}}^{2/9}$. This scaling would arise if $Nu \propto Ra^{2/7}$ (from $Ra_F = NuRa$), as has often been reported

in non-rotating experiments and simulations (see e.g. discussions in Siggia 1994; Grossmann & Lohse 2000). None of our data are consistent with the so-called 'ultimate regime' scaling $Nu \propto (RaPr)^{1/2}$ (e.g. Chavanne et al. 1997), which has been conjectured to apply at very high Ra.

The rotating cases exhibit steeper $Nu(Ra_{\text{F}})$ scalings. Fig. 10 shows a series of cases at fixed $Ta = 10^8$ and a smaller number of cases at $Ta = 10^{11}$. Note that the cases at $Ta = 10^{11}$ are situated at $45°$ rather than $90°$. At moderate Ra_{F} (where Ro_c is small) the dependence of Nu on Ra_{F} appear to be reasonably well described by the overplotted scaling $Nu \propto Ra_{\text{F}}^{3/5}$. At higher Ra_{F}, when rotation is unimportant dynamically (large Ro_c), the $Ta = 10^8$ cases latch on to the non-rotating scalings. The slope of the $Nu(Ra_{\text{F}})$ relation is similar for the cases at $Ta = 10^8$ and 10^{11}. Note that for fixed Ta, increasing Ra_{F} is equivalent to increasing Ra_{F}/Ra_c, so a plot of Nu as a function of Ra_{F}/Ra_c would exhibit the same slope.

This behaviour is consistent with prior results in different settings. For example, the transition from a steep 'rotating' $Nu(Ra)$ relation to a shallower 'non-rotating' one was reported by (King et al. 2009) to occur in plane-layer experiments and accompanying Boussinesq simulations (with fixed temperature and no-slip boundaries); see also discussions in King, Stellmach & Buffett (2013) and Aurnou et al. (2020). Simulations in spherical shells (see discussions in Gastine, Wicht & Aubert 2016; Long et al. 2020b, discussing fixed-temperature, and fixed-flux simulations, respectively) likewise exhibit similar trends.

Interestingly, the $Nu \propto Ra_{\text{F}}^{3/5}$ scaling seen in our rotating cases is in accord with the expectations of rotating MLT (Stevenson 1979; Barker, Dempsey & Lithwick 2014; Currie et al. 2020). The same scaling law also arises in the classical 'CIA balance,' which supposes a dynamical balance between Coriolis, inertial, and buoyancy terms in the momentum equation (Aurnou et al. 2020; Vasil et al. 2021) and in asymptotic theories of convection at low Rossby number (Julien et al. 2012). In these theories, the transport is predicted to follow $Nu \propto (Ra_{\text{F}}/Ra_c)^{3/5} \propto (Ra_{\text{F}}Ta^{-2/3})^{3/5}$, which (upon substituting in the definitions for Ra_{F}, Nu, and Ta) is diffusion-free. This suggests that in the rapidly rotating limit the diffusive boundary layers are playing a less significant role in the heat transport. In dimensional terms, this scaling implies that the entropy gradient in the bulk of the convection zone becomes steeper when rotation is more rapid, scaling as $ds/dz \propto \Omega^{4/5}$, with Ω is the angular velocity.

5.4 Boundary layers and the link to dissipation

The trends explored above arise partly from the varying influence of viscous and thermal boundary layers in our simulations. In this subsection, we explore how the widths and other properties of these boundary layers vary as the supercriticality of the convection, the density stratification, and the rotational influence are changed. We also discuss the manner in which the boundary layers, heat transport, flow amplitudes, and dissipation are linked – and demonstrate explicitly that knowledge of some of these aspects constrains the others.

Many different definitions of the boundary layers have been employed in the literature on Boussinesq convection, but our inclusion of rotation, our use of a fixed-flux thermal boundary condition at the bottom boundary, and our adoption of stress-free velocity boundary conditions together implies that some of these definitions are not relevant (see discussion in Long et al. 2020a). We choose here to adopt the simple method suggested by Long et al. (2020a), defining the width of these layers (near the top and bottom of the domain) to be the points at which the advective and conductive contributions
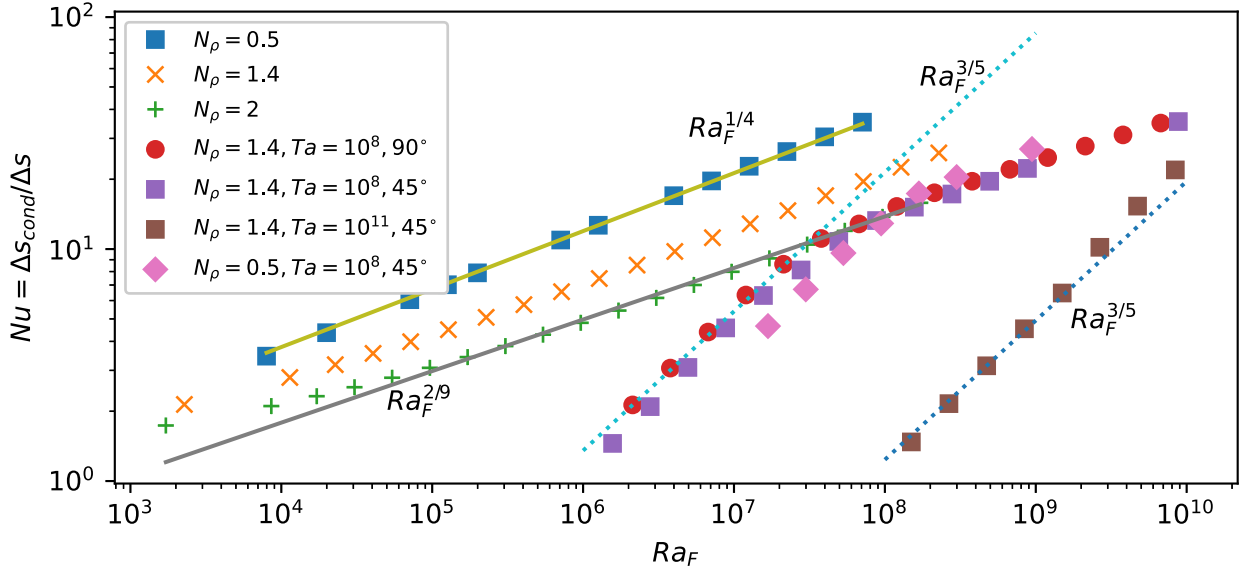
Figure 10. Dimensionless heat transport (Nusselt number) as a function of Ra_F for a sample of rotating and non-rotating cases at different N_ρ.

to the heat transport are equal. Inside the boundary layer conduction dominates the heat transport; outside it convection does. Long et al. (2020a) demonstrate that this method gives sensible results in a variety of Boussinesq settings (with and without rotation), though to our knowledge it has not been previously employed to study anelastic convection simulations.

At the top and bottom boundaries conduction must carry all the energy (because in our simulations the vertical convective velocity goes to zero there, and because near-surface radiative cooling has been ignored). The value of the horizontally averaged entropy gradient $d\langle s\rangle/dz$ at the bottom boundary is therefore determined by the energy flux entering the domain. At the top boundary, the entropy is fixed (rather than its gradient), but in a steady state the simulation must still develop a sufficiently large entropy gradient to carry the same energy flux out the top boundary. Specifically, because we have assumed that conduction diffuses entropy, we must have

$$F = F_{\mathrm{cond}} = -\bar{\rho}\bar{T}\frac{d\langle s\rangle}{dz} \tag{32}$$

at both the top and bottom boundaries. (As elsewhere, all variables here are dimensionless; the dimensional version would have a factor of κ, on the right hand side of the equation.) Because we are considering stratified convection, the density at the top of the domain is smaller than at the bottom, so we expect the entropy gradients $d\langle s\rangle/dz$ that develop will be greater at the outer boundary than at the inner one.

We now suppose that within the conductive boundary layers $d\langle s\rangle/dz$ is approximately uniform, and equal to

$$\frac{d\langle s\rangle}{dz} \approx \frac{\Delta s_{\mathrm{bl}}}{\delta_{\mathrm{bl}}} \approx -\frac{F}{\bar{\rho}\bar{T}} \tag{33}$$

where Δs_{bl} is the entropy jump across the boundary layer and δ_{bl} is its width, $\bar{\rho}$ and $\bar{T}$ are evaluated at the top or bottom of the domain (for the top and bottom boundary layers, respectively), and where we have assumed conduction carries all the flux within the boundary layer.

In Fig. 11 (top panel), we compare the resulting predictions for $\Delta s_{\mathrm{bl}}/\delta_{\mathrm{bl}}$ to measurements in example simulations. We show the ratio of $\Delta s_{\mathrm{bl}}/\delta_{\mathrm{bl}}$ in the bottom boundary layer to that in the top; the
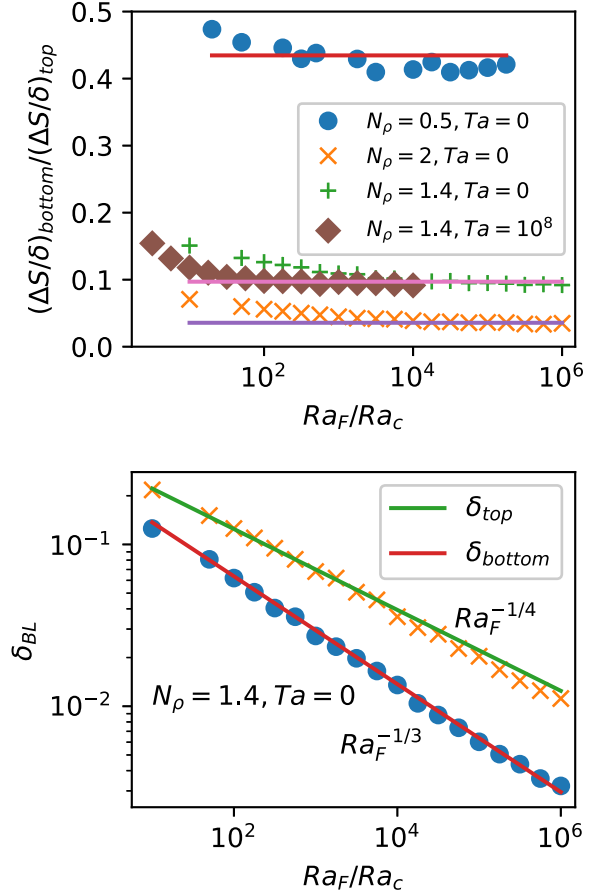
Figure 11. Properties of top and bottom boundary layers at varying Ra_F, N_ρ, and Ta. Top panel shows the ratios of the dimensionless entropy gradients across the bottom and top boundary layers (as defined in the text); bottom panel shows the width of the top and bottom boundary layers in example non-rotating cases at $N_\rho = 1.4$. The horizontal lines show the result of evaluating equation (34) at each stratification.

horizontal lines denote

$$\frac{\bar{\rho}_{\text{top}} \bar{T}_{\text{top}}}{\bar{\rho}_0 \bar{T}_0} \qquad (34)$$

for each stratification, which this ratio should approach (per equation 33, and given that F is the same at both boundaries). The agreement between the measured values and the estimated value is good at high Ra_{F} for all stratifications shown, in both rotating and non-rotating cases. At low Ra_{F}, the agreement is less good. With increasing N_ρ the boundary layers become increasingly asymmetric, so that for example in cases with $N_\rho = 2$, $\Delta s_{\text{bl}}/\delta_{\text{bl}}$ is more than 25 times larger in the top boundary layer than in the bottom. This, again, is a consequence of the much smaller densities and temperatures at the top of these stratified domains, which then require a much larger entropy gradient to carry the imposed flux out the top boundary.

In the bottom panel of Fig. 11, we show how the top and bottom boundary layer widths vary with Ra_{F}, for example, cases at $N_\rho = 1.4$. As expected, the boundary layers grow thinner at higher Ra_{F}. The top and bottom boundary layers appear to follow slightly different trends: We have overplotted $\delta_{bl} \propto Ra_{\text{F}}^{-1/4}$, which appears to match the top boundary layer data well, and $Ra_{\text{F}}^{-1/3}$, which matches the bottom boundary layer well.

These findings are consistent with, and aid in understanding, our findings for the dynamics and heat transport (i.e. $Nu(Ra_{\text{F}})$ scalings) in previous sections. In the non-rotating cases at high Ra_{F} nearly the entire $\Delta\langle s \rangle$ across the whole domain occurs in the top and bottom boundary layers; hence, their width determines the overall Nusselt number for the entire domain. (In rotating cases, the entropy contrast across the bulk can approach or exceed that in the boundary layers; see discussions in, e.g. Barker et al. 2014; Currie et al. 2020.) The top boundary layer is, in our stratified calculations, probably the more restrictive of these because it is thicker; we expect thus expect that in these calculations the Nusselt number should scale approximately as the height of the layer divided by the width of this boundary layer. Here, this implies that Nu should scale as $Ra_{\text{F}}^{1/4}$, which is in agreement with many of our findings for the non-rotating cases in Section 5.3 above.

The steeper heat-transport scalings exhibited by rotating cases are linked to where dissipation occurs. This is because the dissipation and the work done against the background stratification must balance; this balance gives rise to the exact relationship in Boussinesq convection between the $Nu(Ra_{\text{F}})$ relationship and the viscous dissipation (Shraiman & Siggia 2000), and to a more complex analogue of this in the anelastic case (as shown recently by Jones et al. 2022). Changes in where the dissipation occurs – which, in turn, arise because the convective velocities and length-scales change in the presence of rotation, as discussed above – thus also give rise to changes in the heat transport.

This link between dissipation and transport has led some prior authors to separate the viscous dissipation into 'bulk' and 'boundary' contributions – see for example, Grossmann & Lohse (2000), Jones et al. (2022), and Gastine et al. (2016) – and to posit that transitions in the heat transport correspond to changes between bulk-dominated or boundary-dominated dissipation (Grossmann & Lohse 2000). In our simulations, we cannot usefully divide the dissipation in this way; because the boundary layers as defined here become very thin at high $Ra_{\text{F}}/Ra_{\text{c}}$, the dissipation is almost always 'bulk-dominated.' We have argued above that z_{diss} provides, for our setup, a more meaningful distinction between cases where the dissipation is concentrated near the boundaries and those where it is distributed throughout the domain. We find that cases that fall on the rotating scaling relation
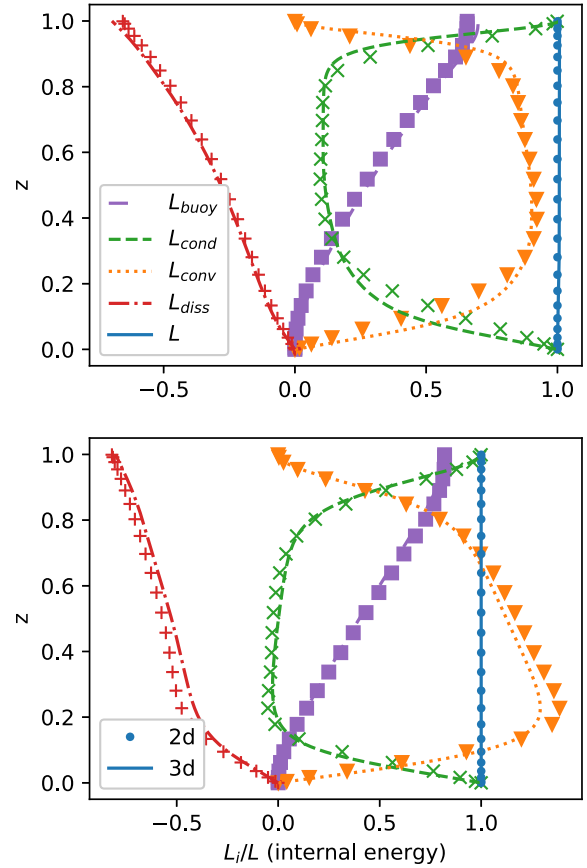
Figure 12. Internal energy transport in rotating (top panel) and non-rotating (bottom panel) cases in both 2D and 3D. The rotating cases are at latitude $45°$.

$Nu \propto (Ra_{\text{F}}/Ra_{\text{c}})^{3/5}$ systematically have larger z_{diss} than those which follow the non-rotating heat transport scalings ($Nu \propto Ra_{\text{F}}^{1/4}$).

5.5 Comparison to fully three-dimensional flows

The simulations presented in the preceding figures were restricted to two spatial dimensions (i.e. assuming axisymmetry in one dimension). In this section, we provide a preliminary view of whether the key quantities assessed in this paper – namely the overall levels of dissipation (as measured by E) and its spatial distribution (as encapsulated by z_{diss} and by the spatial distribution of L_{diss}) – are different in 2D and 3D cases.

In Fig. 12, we examine the energy transport in two example 3D cases and their closest 2D equivalents. We display both non-rotating cases (bottom panel, at $Ra_{\text{F}} \approx 2.3 \times 10^4 \approx 100 Ra_{\text{c}}$) and rotating ones (top panel, at $Ta = 10^6$, $Ra_{\text{F}} = 3.3 \times 10^5 \approx 10 Ra_{\text{c}}$, at 45° latitude). The 2D/2.5D cases have the same Ra_{F} as the 3D ones. All cases have $N_\rho = 1.4$, and an aspect ratio of 2:1 (i.e. the horizontal dimensions extend twice as far as the vertical one). The 3D cases were run at resolutions of $256 \times 256 \times 128$, and evolved for more than a diffusion time. In the figure, data from the 2D cases are overplotted as symbols, with data from the 3D cases as lines.

It is clear that the energy transport in the 3D cases is very similar to that realized in the 2D/2.5D cases. In the non-rotating case, for example, L_{diss} has a steep slope near the lower boundary, and a smaller one in the bulk; this reflects the fact that much of the dissipation is occurring near the lower boundary. In the rotating case, L_{diss} is less sharply

peaked, reflecting the more even distribution of dissipation throughout the bulk. In both cases, the other transport terms (L_{cond}, L_{buoy}, L_{conv}, and the total transport L) are also quite similar in 2D and 3D.

The other bulk quantities of interest to us – E and z_{diss} – are also similar in 2D and 3D. The rotating 3D case shown here has (time-averaged) $E = 0.69$ and $z_{diss} = 0.61$; the corresponding 2.5D case had $E = 0.66$ and $z_{diss} = 0.60$. The non-rotating 3D case has $E = 0.80$ and $z_{diss} = 0.21$; the corresponding 2D case had $E = 0.82$ and $z_{diss} = 0.17$. Crucially, this suggests that in 3D cases, z_{diss} exhibits a similar dependence on rotation as it did in 2.5D: Namely, it is significantly larger when rotation is present (because more of the dissipation is distributed in the bulk in that case) than in the non-rotating case (where much of the dissipation is concentrated near the boundaries).

These results suggest that the key quantities examined in this paper may not be too sensitive to the assumption of axisymmetry. We defer a more detailed study of the 3D cases to later work.

6 DISCUSSION AND CONCLUSIONS

We have presented the first systematic investigation of viscous dissipation in a rotating, stratified plane layer of convection, studied here within the anelastic approximation for an ideal gas. We have shown that, for fixed convective supercriticality Ra_F/Ra_c and moderate stratification, the total dissipative heating does not depend appreciably on rotation rate. However, the spatial *distribution* of the dissipation does vary with rotation, and this has a number of important consequences for the dynamics and heat transport.

The total dissipation is thermodynamically bounded by equation (9), which corresponds to the case in which there is negligible entropy generation by conduction in the bulk of the domain and all the dissipation occurs at the highest possible temperature. In practice, we have not found any cases in which the dissipation exceeded the tighter, empirical bound of equation (10), which does not depend directly on the diffusivities or on rotation rate. Our non-rotating cases, which exhibit simple mono-cellular flows, approach the latter bound at high enough Ra_F/Ra_c. These represent an extreme case in which very little dissipation occurs in the bulk of the convection zone, so we regard them as a limit on E that is unlikely to be exceeded by more realistic flows.

In rotating cases, the viscous dissipation is more uniformly distributed throughout the layer than in corresponding non-rotating cases. In the non-rotating simulations, much of the dissipation occurs near the bottom of the computational domain, so that although there is a global balance between dissipation and work done against the background stratification, these quantities do not balance at each depth. We defined a new quantity z_{diss}, the height at which half the total viscous dissipation has occurred, which encapsulates the spatial distribution of the dissipation in a simple way, and used it to characterize our simulations in different regimes.

We have shown that the heat transport scalings ($Nu(Ra_F)$) in our rotating cases appear to be consistent with theoretical diffusion-free predictions arising from either 'rotating MLT' (Stevenson 1979; Barker et al. 2014; Currie et al. 2020) or, equivalently, from a conjectured balance between Coriolis, inertial, and buoyancy forces (e.g. Gastine et al. 2016; Aurnou et al. 2020; Vasil et al. 2021). Prior work has shown this in other settings (mainly within the Boussinesq approximation).

We have shown that these changes in heat transport are linked to where in the domain the dissipation occurs. This is similar to the case in Boussinesq convection, where prior work (e.g. Grossmann & Lohse 2000) has established that the $Nu(Ra_F)$ heat transport relation varies depending on whether the dissipation is 'bulk' or 'boundary' dominated, and broadly in line with very recent theoretical predictions for the anelastic case (Jones et al. 2022). Here, the situation is more complex than in the Boussinesq case because of the background stratification, but the same basic trends appear to hold. In particular, we find that cases which follow the 'rotating' heat transport relation are those for which z_{diss} is especially high.

We also established that, for the setup examined here, the thermal boundary layers in our simulations are asymmetric – the top one being considerably larger than the bottom – and that the thicknesses of the top and bottom boundary layers scale differently with Ra_F.

Finally, we have explored the link between dissipation and the kinetic energy flux. We developed a simple model of the kinetic energy flux in our non-rotating cases – based on the idea that dissipation approaches the upper bound at high enough Ra_F, and that much of the dissipation occurs near the lower boundary – and showed that it provided a reasonably accurate prediction of the maximum (negative) kinetic energy flux attained in our simulations for each stratification at high enough Ra_F. We have argued that this provides an upper bound on the kinetic energy flux achievable by real convection.

If our results are applicable to real stars, one conclusion is that rapidly rotating stars should exhibit less convective overshooting into adjacent stably stratified regions than slowly rotating ones. From the perspective adopted here, this is because in rotating convection zones the buoyancy work at each depth is more nearly balanced *locally* (rather than just globally) by dissipation. Equivalently, the more rapidly rotating cases have more dissipation per unit volume in the bulk (all else being equal). For a fixed stratification, this will imply (following the discussion in e.g. Anders et al. 2022) that convective motions in rotating stars will have less kinetic energy when they reach the boundary of the Schwarzschild-unstable region, so they will penetrate less deeply into the adjacent layers.

Similarly, we expect a smaller kinetic energy flux in rotating stars and planets than in non-rotating ones. The dynamical consequences of this are not yet clear, but we intend to explore them in the future.

DATA AVAILABILITY

The codes used to produce the simulations in this paper, and selected outputs from the simulations themselves, have been uploaded to the Exeter Open Research repository (ore.exeter.ac.uk) and are available for download there (DOI 10.24378/exe.4945).

REFERENCES

Aboussière T., Ricard Y., 2013, J. Fluid Mech., 725, R1
Aboussière T., Ricard Y., 2014, J. Fluid Mech., 751, 749
Aboussière T., Curbelo J., Dubuffet F., Labrosse S., Ricard Y., 2022, J. Fluid Mech., 940, A9
Anders E. H., Brown B. P., 2017, Phys. Rev. Fluids, 2, 083501
Anders E. H., Manduca C. M., Brown B. P., Oishi J. S., Vasil G. M., 2019, ApJ, 872, 138
Anders E. H., Jermyn A. S., Lecoanet D., Brown B. P., 2022, ApJ, 926, 169
Arnett W. D., Meakin C., Viallet M., Campbell S. W., Lattanzio J. C., Mocák M., 2015, ApJ, 809, 30
Aurnou J. M., Horn S., Julien K., 2020, Phys. Rev. Res., 2, 043115
Backus G. E., 1975, Proc. Natl. Acad. Sci., 72, 1555
Barker A. J., Dempsey A. M., Lithwick Y., 2014, ApJ, 791, 13
Batygin K., Stevenson D. J., 2010, ApJ, 714, L238
Braginsky S. I., Roberts P. H., 1995, Geophys. Astrophys. Fluid Dyn., 79, 1
Browning M. K., Brun A. S., Toomre J., 2004, ApJ, 601, 512
Browning M. K., Weber M. A., Chabrier G., Massey A. P., 2016, ApJ, 818, 189
Brun A. S., Browning M. K., 2017, Liv. Rev. Solar Phys., 14, 4
Burns K. J., Vasil G. M., Oishi J. S., Lecoanet D., Brown B. P., 2020, Phys. Rev. Res., 2, 023068
Canuto V. M., 1997, ApJ, 489, L71
Chandrasekhar S., 1961, Hydrodynamic and hydromagnetic instability. International Series of Monographs on Physics, Oxford:Clarendon
Chavanne X., Chillà F., Castaing B., Hébral B., Chabaud B., Chaussy J., 1997, Phys. Rev. Lett., 79, 3648
Currie L. K., Browning M. K., 2017, ApJ, 845, L17 (CB17)
Currie L. K., Barker A. J., Lithwick Y., Browning M. K., 2020, MNRAS, 493, 5233
Featherstone N. A., Hindman B. W., 2016, ApJ, 818, 32
Gastine T., Wicht J., Aubert J., 2016, J. Fluid Mech., 808, 690
Gilman P. A., 1978, Geophys. Astrophys. Fluid Dyn., 11, 157
Ginet G. P., 1994, ApJ, 429, 899
Gough D. O., Weiss N. O., 1976, MNRAS, 176, 589
Grossmann S., Lohse D., 2000, J. Fluid Mech., 407, 27
Hewitt J. M., McKenzie D. P., Weiss N. O., 1975, J. Fluid Mech., 68, 721 (HMW75)
Hindman B. W., Featherstone N. A., Julien K., 2020, ApJ, 898, 120
Hurlburt N. E., Toomre J., Massaguer J. M., 1984, ApJ, 282, 557
Ireland L. G., Browning M. K., 2018, ApJ, 856, 132
Jarvis G. T., McKenzie D. P., 1980, J. Fluid Mech., 96, 515
Jermyn A. S., Anders E. H., Lecoanet D., Cantiello M., 2022, ApJS, 262, 19
Jones C. A., Mizerski K. A., Kessar M., 2022, J. Fluid Mech., 930, A13
Julien K., Knobloch E., Rubio A. M., Vasil G. M., 2012, Phys. Rev. Lett., 109, 254503
Kaspi Y. et al., 2018, Nature, 555, 223
Kaspi Y., Galanti E., Showman A. P., Stevenson D. J., Guillot T., Iess L., Bolton S. J., 2020, Space Sci. Rev., 216, 84
Kazemi S., Ostilla-Mónico R., Goluskin D., 2022, Phys. Rev. Lett., 129, 024501
King E. M., Stellmach S., Noir J., Hansen U., Aurnou J. M., 2009, Nature, 457, 301
King E. M., Stellmach S., Buffett B., 2013, J. Fluid Mech., 717, 449
Kulsrud R. M., 2005, Plasma Physics for Astrophysics. Princeton University Press, Princeton, NJ
Kupka F., Ahlborn F., Weiss A., 2022, A&A, 667, A96
Lantz S. R., 1992, PhD thesis, Cornell University
Lecoanet D., Brown B. P., Zweibel E. G., Burns K. J., Oishi J. S., Vasil G. M., 2014, ApJ, 797, 94
Liu J., Goldreich P. M., Stevenson D. J., 2008, Icarus, 196, 653
Long R. S., Mound J. E., Davies C. J., Tobias S. M., 2020a, Phys. Rev. Fluids, 5, 113502
Long R. S., Mound J. E., Davies C. J., Tobias S. M., 2020b, J. Fluid Mech., 889, A7
Malkus W. V. R., 1954, Proc. R. Soc. Lond. Ser. A, 225, 196
Meakin C. A., Arnett W. D., 2010, Ap&SS, 328, 221
Mizerski K. A., Tobias S. M., 2011, Geophys. Astrophys. Fluid Dyn., 105, 566
Nicoski J. A., O'Connor A. R., Calkins M. A., 2023, preprint (arXiv:2308.05174)
Oishi J., Burns K., Clark S., Anders E., Brown B., Vasil G., Lecoanet D., 2021, J. Open Source Softw., 6, 3079
Priest E., 2014, Magnetohydrodynamics of the Sun. Cambridge University Press, Cambridge, UK
Rogers T. M., Glatzmaier G. A., Woosley S. E., 2003, Phys. Rev. E, 67, 026315
Shraiman B. I., Siggia E. D., 2000, Nature, 405, 639
Siggia E. D., 1994, Annu. Rev. Fluid Mech., 26, 137
Stein R. F., Nordlund A., 1989, ApJ, 342, L95
Stevenson D. J., 1979, Geophys. Astrophys. Fluid Dyn., 12, 139
Vasil G. M., Julien K., Featherstone N. A., 2021, Proc. Natl. Acad. Sci., 118, e2022518118
Viallet M., Meakin C., Arnett D., Mocák M., 2013, ApJ, 769, 1
Wang Q., Chong K. L., Stevens R. J. A. M., Verzicco R., Lohse D., 2020, J. Fluid Mech., 905, A21

SUPPORTING INFORMATION

Supplementary data are available at *MNRAS* online.

Table 1. Input parameters and selected output quantities for example simulations presented in this paper.

Please note: Oxford University Press is not responsible for the content or functionality of any supporting materials supplied by the authors. Any queries (other than missing material) should be directed to the corresponding author for the article.

This paper has been typeset from a TEX/LATEX file prepared by the author.